

# Exploring relaxation dynamics in warm dense plasmas by tailoring non-thermal electron distributions with a free electron laser

Y.-F. Shi (石元峰),<sup>1,\*</sup> S. Ren (任申元),<sup>2</sup> H.-K. Chung,<sup>3</sup> J. S. Wark,<sup>1</sup> and S. M. Vinko,<sup>1,4</sup>

<sup>1</sup>*Department of Physics, Clarendon Laboratory, University of Oxford, Parks Road, Oxford, OX1 3PU, UK*

<sup>2</sup>*Beijing Jiaotong University, Beijing, China*

<sup>3</sup>*Korea Institute of Fusion Energy, Daejeon, 34133, Republic of Korea*

<sup>4</sup>*Central Laser Facility, STFC Rutherford Appleton Laboratory, Didcot OX11 0QX, UK*

(Dated: May 24, 2024)

Knowing the characteristic relaxation time of free electrons in a dense plasma is crucial to our understanding of plasma equilibration and transport. However, experimental investigations of electron relaxation dynamics have been hindered by the ultra-fast, sub-femtosecond time scales on which these interactions typically take place. Here we propose a novel approach that uses x-rays from a free electron laser to generate well-defined non-thermal electron distributions, which can then be tracked via emission spectroscopy from radiative recombination as they thermalize. Collisional radiative simulations reveal how this method can enable the measurement of electron relaxation time scales *in situ*, shedding light on the applicability and accuracy of the Coulomb Logarithm framework for modelling collisions in dense plasmas.

## I. INTRODUCTION

Warm dense matter (WDM), with a typical density of a solid and a temperature of 10s of eV, is of fundamental interest as it underpins a broad range of processes in planetary science [1, 2], astrophysics [3], and inertial confinement fusion applications [4]. Despite its significance, understanding its transport properties, such as radiation transport or thermal and electron conductivity, remains challenging [5, 6]. This is not only because the ultrafast electron relaxation processes that govern these properties take place on sub-fs time scales, but also because of the strong Coulomb coupling in dense charged-particle systems.

In a dense plasma, the principal mechanism underlying most relaxation and equilibration processes stems from collisional charged particle interactions. The relaxation time of free electrons,  $\tau_e$ , is the key parameter that characterises electron relaxation. Generally, this parameter is determined by four contributions: electron-electron (e-e) collisions, electron-ion (e-i) collisions, electron-natural-atom (e-n) collisions and electron-phonon scattering. While there is no general consensus on how all these processes should be described in a computationally efficient way for a generic dense plasma system, much effort has been dedicated to deriving analytical expressions for these collisional terms across various regimes of interest [7–10].

Electron-phonon scattering is commonly assumed to be negligible in warm dense matter systems [11], and the other three contributions will dominate the relaxation process. Nevertheless, electron-phonon interactions could still be important in certain laser-produced plasmas, especially during plasma creation [12], and models can be constructed to account for such interactions,

e.g. via the Boltzmann transport equation assuming near-equilibrium [13]. The contribution of e-n collisions, while not negligible, is generally believed to be well understood, and accepted cross-section models have been widely adopted in the literature [5, 11].

In contrast to the two processes mentioned above, modelling e-i and e-e collisions poses a more substantial challenge in the WDM regime. For weakly coupled systems, they are commonly described as binary processes, assuming that cumulative small-angle collisions dominate hard Coulomb collisions. With this assumption, the interaction can be described in terms of a Coulomb logarithm (CL), which in various forms dictates collision frequencies in plasmas [14, 15]. However, this assumption fails for moderately or strongly coupled systems, where strong collisions and many-body interactions become important. At high densities, the argument of the CL tends to zero, leading to a divergence in the collisional rates, thus necessitating revised models or new approaches altogether. Despite these limitations, the simplicity of the classical CL model remains appealing, and continues to be widely used in simulation codes today [16].

There have been several attempts to correct the CL to allow it to be used at high densities. Some of the most recent attempts that still operate under the semi-classical Coulomb potential scattering (or Yukawa potential scattering) include applying Born's approximation to cylindrical screening [15], or applying partial wave analysis [8, 17]. Beyond the semi-classical framework, there have also been quantum treatments, both within the framework of linear response theory [18–22] and by making use of other advanced methods [23–26].

A rich collection of theoretical approaches to the modelling of the CL, and of collisions more generally, has been developed over the past few decades. However, the validation of these models is severely hampered by the lack of experimental measurements of electron interaction dynamics and relaxation time scales in high-density systems. Very few attempts have been made to mea-

\* yuanfeng.shi@physics.ox.ac.uk

sure the electron relaxation time experimentally. Sun *et al.* reported a measured value of  $\tau_e \approx 1.7$  fs in fused silica [27] by measuring the plasma opacity in a pump-probe experiment. This method was developed by Pan *et al.* [28] to investigate the opacity dependence on electron density, but was limited to densities below that of a solid. Generally, there is little data for systems at densities around or exceeding that of a typical solid. It is worth stressing that determining plasma opacities is in and of itself a challenging problem in the warm-dense matter regime [29, 30], and the use of such data to infer collisional rates is often heavily model-dependent [31, 32].

In recent years, x-ray Free Electron Lasers (XFELs) have proven capable of creating matter under extreme conditions of temperature, pressure, and density [33–36]. Specifically, plasmas with a temperature of 100s of eV and remaining at exactly solid density have been created at LCLS by isochorical x-ray heating: during a typical  $\sim 30$  fs XFEL pulse, the sample has no time to expand, and thus remaining at its original solid density, facilitating the study of transient warm dense plasmas in well-defined thermodynamics conditions [37]. Interestingly, the x-ray-matter interaction process by which samples are isochronally heated by an XFEL is via x-ray absorption and the generation of copious amounts of non-thermal electrons, either directly via photoionization or indirectly through Auger decay [38]. While the electrons subsequently collide and their distribution thermalizes, they also recombine into core holes, thus emitting photons that encode their distribution. By observing the emission spectrum from such non-thermal electrons, information regarding the electron distribution function and the characteristic relaxation time can thus be revealed.

Here, we propose an experimental method to make use of this physical process to explore electron relaxation dynamics. Our approach focuses on tracking the evolution of non-thermal electrons within a broader electron distribution in a dense plasma on ultrafast time scales. This is achievable through the use of an XFEL, which can photoionize core electrons from atoms in a plasma, resulting in sustained and, importantly, well-defined non-thermal electron distributions. We present simulations conducted using the CCFLY collisional-radiative atomic kinetics code [36, 38–40]. Our results indicate that adjusting the XFEL pulse duration from sub-femtosecond to a few femtoseconds enables a measurement of the relaxation time scale of non-thermal electrons in the plasma, allowing us to glean insights into electron interaction processes on ultra-fast time scales and to assess the validity of the Coulomb Logarithm framework to describe dense plasma systems more generally.

## II. METHOD

When a sample is exposed to an XFEL beam with photon energy exceeding the  $1s$  ionization energy (i.e., above

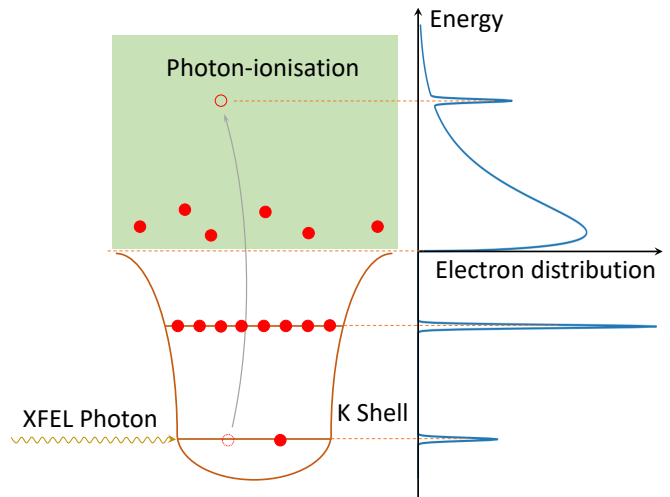


FIG. 1. When a sample is driven by an intense x-ray pulse, K-shell photoionization and Auger decay create copious populations of non-thermal electrons at well-defined energies. These electrons thermalize collisionally with ions and other electrons in the system on electron equilibration time scales.

the K-edge), the main absorption mechanism is K-shell photoionization (PI). In a low-Z element, the dominant relaxation of a  $1s$  core hole takes place via Auger decay, which further excites an electron from a bound state into the continuum. These processes produce free electrons with well-defined energies, leading to non-thermal peaks in the electron energy distribution, as illustrated in Fig. 1. The non-thermal electrons created by this method thermalize rapidly yet are continuously replenished within the pulse duration of the driving XFEL beam. Therefore, there is a non-negligible probability for the non-thermal electrons to radiatively recombine into a core hole before the electron distribution fully equilibrates. Because the dominant radiative recombination channel will be into a  $1s$  state, the emitted photons will have energies corresponding to the K-edge plus the energy of the free electron in the non-thermal distribution. As illustrated in Fig. 2, we can distinguish two main cases: recombination from PI electrons, with emitting photon energies similar to that of the driving x-ray pulse, and recombination of Auger-excited electrons, emitted at energies twice the  $K_\alpha$  energy.

Radiative recombination to the K shell can only take place in the presence of a K-shell core hole. These core holes are predominately produced through photon-ionization, with only a small fraction produced by collisional ionization due to the relatively low temperature compared with the K shell ionisation energy. Since these holes are majorly created by the XFEL beam, the X-ray pulse duration will determine the window within which emission can be observed. For a pulse length shorter than the relaxation time (typically below 1 fs), the majority of the emission will occur before significant thermalization can happen, leading to a strong non-thermal signature in

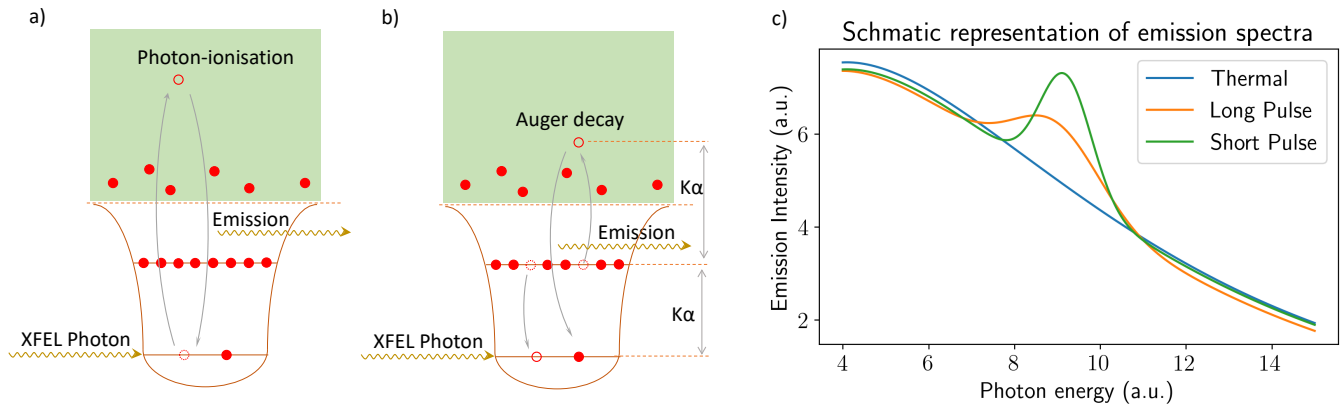


FIG. 2. Emission from non-thermal electrons features prominently at photon energies corresponding to the process that created the non-thermal electrons. (a) Quasi-elastic: an electron photoionized from the K-shell recombines back into the K-shell, emitting a photon with energy approximately equal to the incident XFEL photon energy. (b) Auger: the non-thermal electrons created by Auger processes recombine, emitting a photon with twice the energy of a K $\alpha$  photon. Other processes, such as L-shell photoionization/recombination, are also possible but have a much lower cross-section. (c) Illustration of the dependence of the non-thermal feature as seen in emission as a function of XFEL pulse duration.

the emission spectrum. In contrast, if the XFEL beam delivers the same number of photons but over a considerably longer pulse duration, a larger proportion of emission will take place from more thermalized electron distributions, leading to a weaker non-thermal signature in the emission spectrum. By varying the pulse duration to lie between these two limits, we can thus experimentally explore the electron equilibration process in a dense plasma. The ability of XFELs to deliver quasi-monochromatic x-ray pulses with durations ranging from sub-fs to several 10's of fs thus makes them uniquely suited for probing electron relaxation times and, in particular, experimentally validating electron relaxation and transport models in dense plasmas.

### A. Simulations

We model the x-ray-matter interaction process using CCFLY [38], a non-LTE (local thermodynamic equilibrium) atomic-kinetics collisional-radiative code based on the popular SCFLY [40, 41] and FLYCHK [39] simulation suites previously used to model isochoric heating experiments at XFEL facilities [36]. Of importance to this work, CCFLY includes a Fokker-Planck solver for the free electron distribution function, which is coupled to the full non-LTE atomic kinetics framework. This allows us to model the time evolution of the electrons directly during the ultrafast x-ray isochoric heating process, and to compute a time-dependent emission spectrum self-consistently. The CCFLY code tracks the atomic level populations as a function of time during the x-ray irradiation process, taking into account the full range of transitions between levels, including electron capture, collisional ionization and recombination, collisional transition, stimulated transitions, photo-ionization, inverse

bremsstrahlung, and radiative recombination [39]. For processes involving free electrons, the transition rates make use of the non-thermal electron distribution function  $f[E, t]$ . The evolution of the electron distribution is determined by three components: the elastic collision term  $\hat{O}_e[f]$ , the inelastic collision term  $\hat{O}_i[f]$ , and a source term  $S$  that accounts for ionization and recombination processes which do not conserve particle number. The model is zero-dimensional, so it does not account for any spatial extent of the system modelled. The charge state populations and the free electrons are thus modelled purely in terms of densities. In this model, the Boltzman-Vlasov equation for the evolution of the electron distribution is reduced to:

$$\frac{\partial f}{\partial t} = \hat{O}_e[f] + \hat{O}_i[f] + S. \quad (1)$$

The detailed forms of these terms can be found in refs. [38, 42], and references therein. Here, we only highlight that the thermalization is driven by both electron-electron (e-e) collisions and electron-ion (e-i) collisions. We will want to explore the importance of each of these terms to the overall equilibration process.

Because e-e collisions conserve energy of the free electron system, the effect of this process is completely captured by the elastic collision term  $\hat{O}_e[f]$ . This term is evaluated in the velocity space rather than energy space ( $f[E]dE = \varrho[v]dv$ ), and adopts the standard Fokker-Planck formalism [16, 43–45]:

$$\left( \frac{\partial \varrho[v]}{\partial t} \right)_{ee} = \frac{4\pi\Gamma_{ee}}{3} \frac{1}{v^2} \frac{\partial}{\partial v} \left[ \frac{1}{v} \frac{\partial W[\varrho, v]}{\partial v} \right], \quad (2)$$

with

$$W[\varrho, v] = \varrho[v] \int_0^v \varrho[v'] v'^4 dv' + v^3 \varrho[v] \int_v^\infty \varrho[v'] v' dv' - 3 \int_v^\infty \varrho[v'] v' dv' \int_0^v \varrho[v'] v'^2 dv', \quad (3)$$

and  $\Gamma_{ee}$  given by

$$\Gamma_{ee} = \frac{q_e^4 \ln[\Lambda_{ee}]}{4\pi\epsilon_0^2 m_e^2}, \quad (4)$$

where  $\epsilon_0$  is the vacuum permittivity,  $m_e$  the mass of the electron,  $q_e$  the elementary charge, and  $\ln[\Lambda_{ee}]$  the Coulomb logarithm for e-e collisions.

The effect of e-i collisions is, instead, captured by all three terms in Eq. (1). Bremsstrahlung and inverse Bremsstrahlung are (semi-)elastic e-i collisions that do not change the atomic state of the ion. Therefore, they are captured by the elastic collision operator  $\hat{O}_e[f]$ . Collisional excitations and de-excitations, in turn, do not conserve the kinetic energy of the e-i system and are included in the inelastic operator  $\hat{O}_i[f]$ . Collisional ionization and recombination do not conserve the number of electrons, so they are captured by the source term  $S$ .

While the x-ray isochoric heating process occurs on fs timescales, the equilibration timescale between electrons and ions is much longer, on the order of several ps. For the purposes of this work, we can, therefore, assume the ions are stationary and thus neglect the contribution of elastic e-i collisions. We adopt the cross-section model by Lotz [46] for collisional ionization and recombination, and that of Van Regenmortel [47] for collisional excitation and de-excitation. Radiative recombination and dielectronic recombination, though induced by e-i collisions, do not thermalize the electron distribution but only point-wisely subtract electrons at certain energies. They are thus captured by the source term  $S$  in our simulation. Interestingly, e-e and e-i collisions thermalize the non-thermal electrons in two different ways. Typically, e-e collisions only change the energy of the electrons by a small amount per collision, but e-i collisions can remove a large amount of energy at a time. Intuitively, e-e collisions will thus tend to cause non-thermal peaks in the electron distribution to broaden while largely conserving the total number of electrons within it. In contrast, e-i collisions act to depopulate the non-thermal electron peaks but cause little broadening.

The kinetic simulation computes the evolution of the atomic-level populations and of the electron distribution function  $f[E, t]$ . From these, the emissivity and opacity, and hence the time-dependent emission spectrum of the system, can be calculated. Integrating the emission over the duration of the X-ray pulse provides the observable that can, in principle, be measured experimentally. We note that Eq. (4) establishes a connection between the spectral emission from a system irradiated with x-rays of some given pulse duration and the collisional model

setting the electron relaxation time scale. For example, in the Spitzer and Härm model [14], the relaxation time for e-e collisions is:

$$\tau_{ee} = 16 \sqrt{\frac{2}{\pi}} \frac{m_e^{1/2} \epsilon_0^2 (k_B T_e)^{3/2}}{n_e q_e^4 \ln[\Lambda_{ee}]}, \quad (5)$$

where  $k_B$  is the Boltzmann constant,  $T_e$  is the effective electron temperature, and  $n_e$  is the electron density. The simulated emission spectrum is thus determined by the speed of relaxation given by Eq. (2), dependent on the Coulomb logarithm given by Eq. (4), which can be linked to a relaxation time via Eq. (5). In this work, we use Huba's expression for the e-e Coulomb logarithm [48]. However, our Fokker-Planck treatment is compatible with other approaches and can be used to assess different Coulomb logarithm models.

### III. RESULTS

We first simulate the interaction of a 10  $\mu\text{m}$  thick Al foil with an x-ray pulse with photon energy  $\hbar\omega_0 = 2000$  eV, pulse duration of 0.5 fs, and a peak intensity of  $10^{19}$   $\text{Wcm}^{-2}$  on target. The Al K-edge is located at  $E_{1s} = 1560$  eV, so the photons carry sufficient energy to ionize the 1s electrons. Our chosen focus spot sizes of 1  $\mu\text{m}^2$  allow for the heating of solid density plasmas to electron temperatures of  $\sim 70$  eV.

We plot the evolution of the electron distribution in Fig. 3. We see clear non-thermal features corresponding to electrons ejected into the continuum via K- and L-shell photoionization and from Auger decay processes on ultrafast time scales. The simulated XFEL pulse reaches its peak at 1.0 fs, and its temporal and spectral profile is assumed to be a Gaussian. We note that combined XFEL conditions used in these simulations have not yet been achieved together at an XFEL facility. However, each individual parameter (intensity, pulse duration, photon number) is readily achievable today [49], and jointly, they are likely to become possible in the near future.

From Fig. 3, we see that as the intensity of the XFEL beam gradually increases and reaches its peak at 1.0 fs, two PI channels and one Auger channel continuously produce non-thermal electrons. Electrons that are ionised from the K-shell sit at  $E = \hbar\omega_0 - E_{1s} \approx 440$  eV, and those from the L-shell sit at  $\approx 1900$  eV. As the intensity of the X-ray pulse rises, an increasing number of K-shell core holes are created in the Al sample. The presence of a core hole increases the K-edge energy by some 170 eV. Thus, we see the appearance of a small satellite peak at around 270 eV in Fig. 3 and at times after 0.6 fs. The electrons created by KLL Auger decay around 1400 eV also exhibit multiple peaks in the electron distribution, corresponding to photoelectrons emitted from different charge states. Furthermore, at  $t = 1$  fs a small peak occurs above 2 keV, which is not created by direct PI but rather by collisional K $\rightarrow$ L de-excitations that transfer

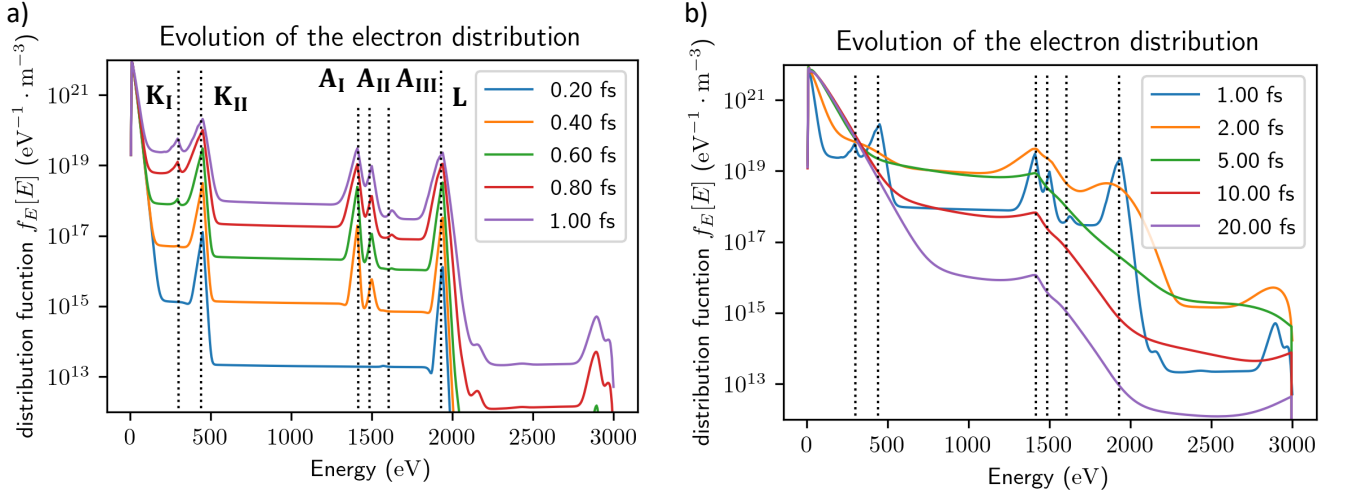


FIG. 3. Evolution of the non-thermal electron distribution. (a) Non-thermal electrons are created via photoionization and Auger decay in the first fs of the pulse. (b) the electron distribution function thermalized to equilibrium after the x-ray pulse peaked at 1 fs.

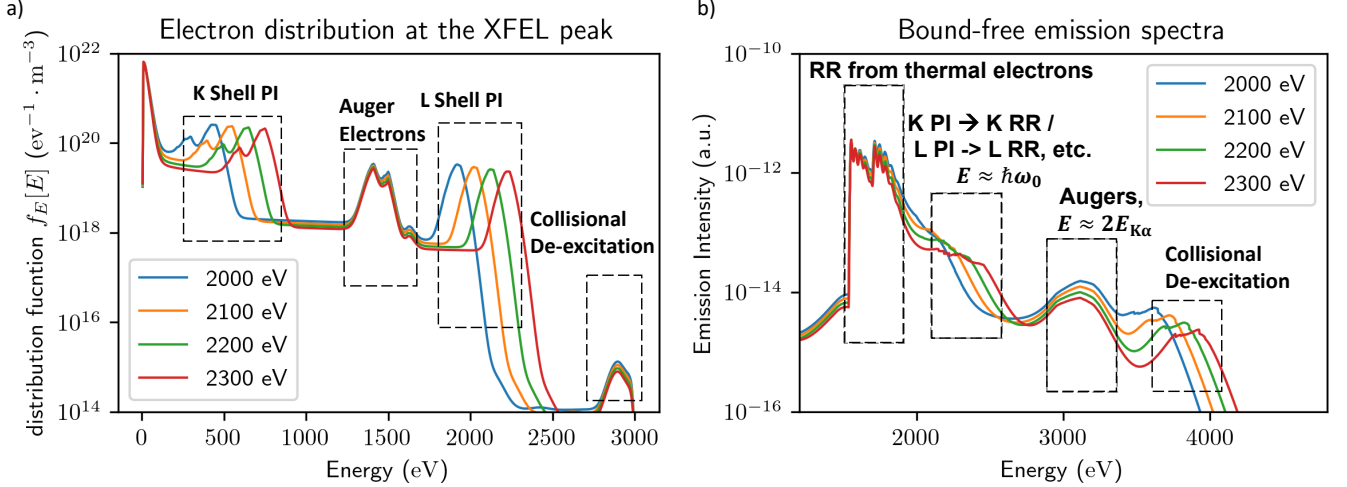


FIG. 4. Tailoring non-thermal electron distributions by tuning the XFEL photon energy. (a) The distribution function of electrons when XFEL pulses reach peak intensities. The energies of the PI electrons are shifted by the same amount as the XFEL photon energy, while the Auger electrons are always created at the same energy. (b) The bound-free emissions from PI electrons shift accordingly, while the peaks due to Auger electrons remain unchanged.

energy to the free electrons. This mechanism is also responsible for producing the highest energy feature near 3 keV. We note that these features are weak — some four orders of magnitude weaker than those due to PI. It is unlikely that such features could easily be observed experimentally. The various processes generating non-thermal electrons are listed in Table I, where electrons are labelled as K, L or A according to the producing mechanism (K-shell photoionization, L-shell photoionization, Auger decay), and Roman numerals denote peaks arising from different ion configurations.

The ability to tailor the electron distribution function is essential for measuring electron relaxation time scales.

TABLE I. Energy of non-thermal electrons, as shown in Fig. 3.  $K^m L^n$  denotes ion configuration of  $m$  electrons in the K shell and  $n$  in the L shell.  $x$  and  $y$  in this table refer to arbitrary integer numbers.

Electron Label	Energy (eV)	Producing Process
$K_I$	270	PI: $K^2 L^y \rightarrow K^1 L^y$
$K_{II}$	440	PI: $K^1 L^y \rightarrow K^0 L^y$
$A_I$	1410	AD: $K^1 L^8 \rightarrow K^2 L^6$
$A_{II}$	1500	AD: $K^1 L^7 \rightarrow K^2 L^5$
$A_{III}$	1625	AD: $K^0 L^8 \rightarrow K^1 L^7$
$L$	1900	PI: $K^x L^y \rightarrow K^x L^{y-1}$

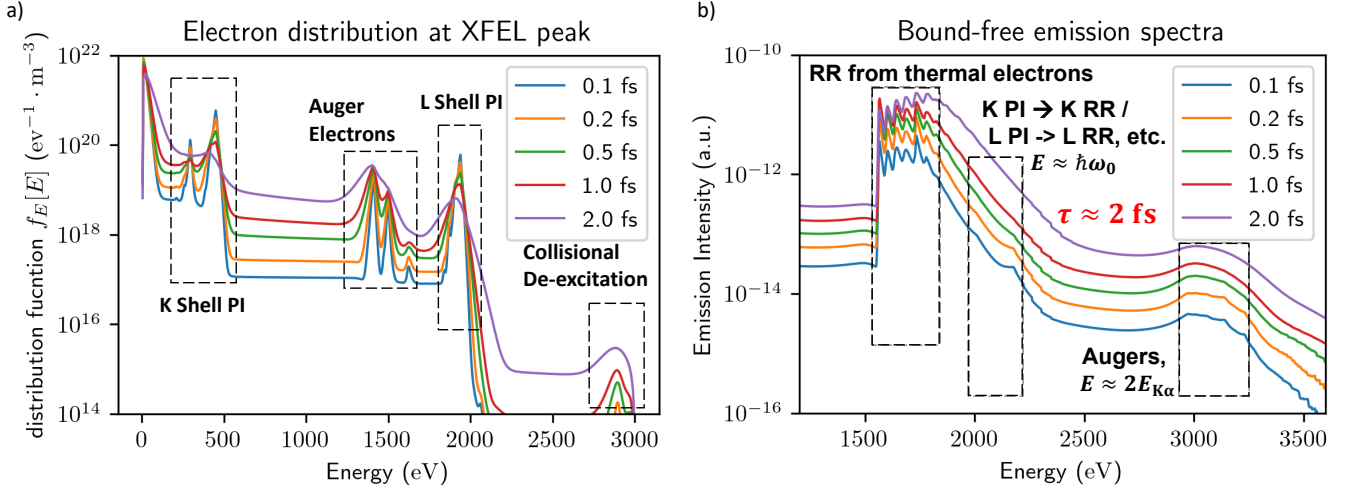


FIG. 5. Effect of XFEL pulse duration on the emission spectrum at constant pulse energy. a) The electron distribution when the XFEL intensity reaches its peak shows that for longer pulse durations, the electron distribution has been significantly thermalized. (b). Corresponding bound-free emission spectra show that the non-thermal feature vanishes when the pulse duration is long. Please note that we have used different normalisations for different pulse durations on the  $y$ -axis to provide a clearer comparison. The actual intensity of the emission spectra is similar across various pulse durations.

We show that the non-thermal electron distribution is easily altered by tuning XFEL photon energy: the energies of the PI electrons are shifted by the same amount of the XFEL photon energy shift while the Auger decay peaks remain unchanged. This is a useful experimental technique because one needs to distinguish various emission signals in the emission spectrum and identify which features are exclusively due to non-thermal electrons.

We illustrate this capability with a set of simulations. The XFEL photon energy was set to 2000 eV in the first simulation and then gradually increased in 100 eV steps to 2300 eV in the following simulations. In each case, the XFEL reaches its peak intensity at  $t = 0.5$  fs. The pulse duration of this set of simulations is 0.2 fs, and they are run for 1 fs, so the electrons do not undergo significant thermalization, and the emission spectra exhibit strong non-thermal features which are easily tracked in energy. We show in Fig. 4 that as the XFEL photon energies increase, the energies of the PI electrons are shifted by the same amount. In contrast, the energy of the Auger electrons remains the same as the KLL Auger electron energy depends only on the K shell and the L shell binding energies. The peaks are less pronounced at higher photon energies because the cross sections for absorption and emission are lower.

### A. Changing pulse duration

We now proceed to investigate the emission spectrum as a function of varying pulse duration. We expect that an increased pulse duration will dampen the non-thermal features in the emission spectrum as the electron distributions thermalize, and we quantify this effect through

non-thermal atomic kinetics simulations.

We simulate x-ray pulses with a fixed pulse energy of  $20 \mu\text{J}$  and a photon energy of 2000 eV. The pulse durations are varied between 0.2 fs and 2 fs, leading to a range of different thermalization timescales and x-ray intensities on target, with the highest corresponding to  $1 \times 10^{19} \text{Wcm}^{-2}$ . The simulation window is 40 fs, chosen to allow enough time for electron thermalization to take place. The emission spectra are shown in Fig. 5, and are integrated over the entire duration of the pulse. They are thus representative of spectra that would be collected experimentally. We see that because longer pulses sample more extended periods of electron thermalization, they exhibit smoother electron distributions and emission spectra compared with the sharper features visible for the shortest pulses. For the shortest 0.2 fs pulse, the emission peaks from PI and Auger electrons, including the satellite peaks, are clearly defined. For the pulses around 1 fs, the peaks are still visible, but due to extensive electron thermalization, they start to wash out for pulse durations above 2 fs. This serves as clear evidence that the relaxation process can be revealed by changing the pulse duration. As the energy of this set of simulations is kept constant, the electrons gain approximately the same energy across the various pulse durations and reach overall temperatures of around 70 eV. The relaxation time given by Eq. (5) is 0.2 fs.

### B. Electron-electron and electron-ion collisions

In the preceding section, we showed how we can track the relaxation of the electron distribution function by varying the pulse duration of the XFEL. This process,



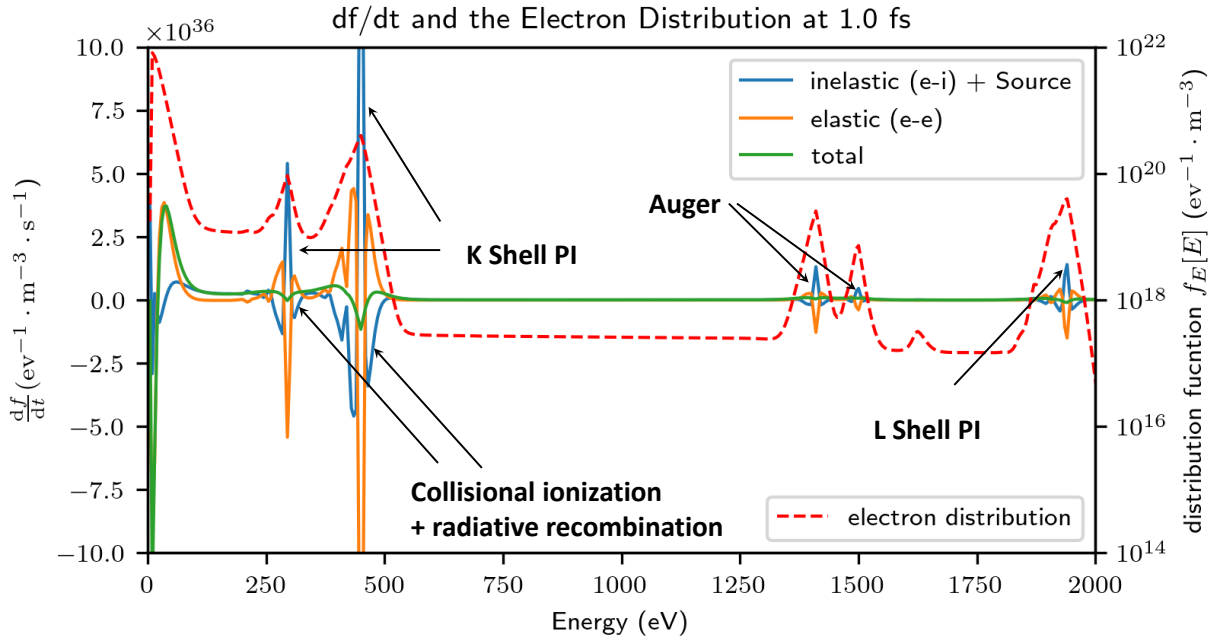


FIG. 6. Contribution of e-e collisions to  $\frac{\partial f}{\partial t}$  compared to that of e-i collisions and source term. The two components thermalize the electron distribution differently, but the overall magnitude is similar.

however, includes the contributions of both e-i and e-e collisions, both of which thermalize the distribution, but in different ways. To better understand their relative roles we shall now examine how the electron distribution function changes in time due to these two types of collisions. The simulation corresponds to 10  $\mu\text{m}$  thin Al foil irradiated by an x-ray pulse with a photon energy of 2000 eV, pulse duration of 0.5 fs, and a peak intensity of  $10^{19} \text{ Wcm}^{-2}$ . The first derivative of the electron distribution function  $\frac{\partial f}{\partial t}$  is shown at peak intensity in Fig. 6, split into the two contributions. We note that the e-e contribution to  $\frac{\partial f}{\partial t}$  is negative at the centres of the non-thermal peaks, but positive in the outer wings. These collisions tend to transfer relatively small amounts of energy, and their effect is thus gradually to broaden the non-thermal peaks. In contrast, the combined effect of inelastic collisions and the source term, which include both e-i collisions and photoionization and radiative recombination (PI/RR), manifest differently. Here, the contribution is positive at the centre of the peak, due to non-thermal electron generation via PI or Auger processes. In the surrounding areas, the contribution turns negative as collisional ionization and recombination redistribute the non-thermal electrons.

The effect of collisional processes on the electron distribution and on the observed spectrum can be further explored by selectively deactivating them in the atomic kinetics simulations and in computing the emission spectrum. We show these results in Fig. 7. When only e-e collisions are active, we note that the shape of the non-thermal peaks in the distribution function remains simi-

lar to those calculated with the full simulation, with the only notable difference being their overall intensity. In turn, e-i collisions are critical to redistributing energy away from the non-thermal peaks across a wide energy range, as we observe in the region around 800 eV, far from the K-shell photoionization and Auger features. Here, e-e collisions play a negligible role in the overall equilibration. Similarly, e-i collisions only have a minor effect in determining the shape of the non-thermal peaks, which are, instead, predominantly broadened by e-e collisions.

A similar observation can be made for the emission spectrum, shown in Fig. 7b. We see that the e-i collisions predominantly redistribute the non-thermal electrons across a wide energy range, filling in the gaps between the various groups of non-thermal features, whereas the e-e collisions broaden the non-thermal features, producing a smooth emission spectrum.

### C. Effect of e-e relaxation time scales

We now explore how different electron relaxation timescales, particularly for e-e collisions, affect the spectral emission. These timescales are important in determining relaxation and transport in warm-dense plasmas, and such a comparison sheds light on how these processes are impacted by the accuracy of collisional models, often described in terms of a Coulomb Logarithm. We have already shown that the pulse duration of an XFEL largely determines the shape of the emission spectrum. Thus, we can imagine an experiment where multiple pulse du-

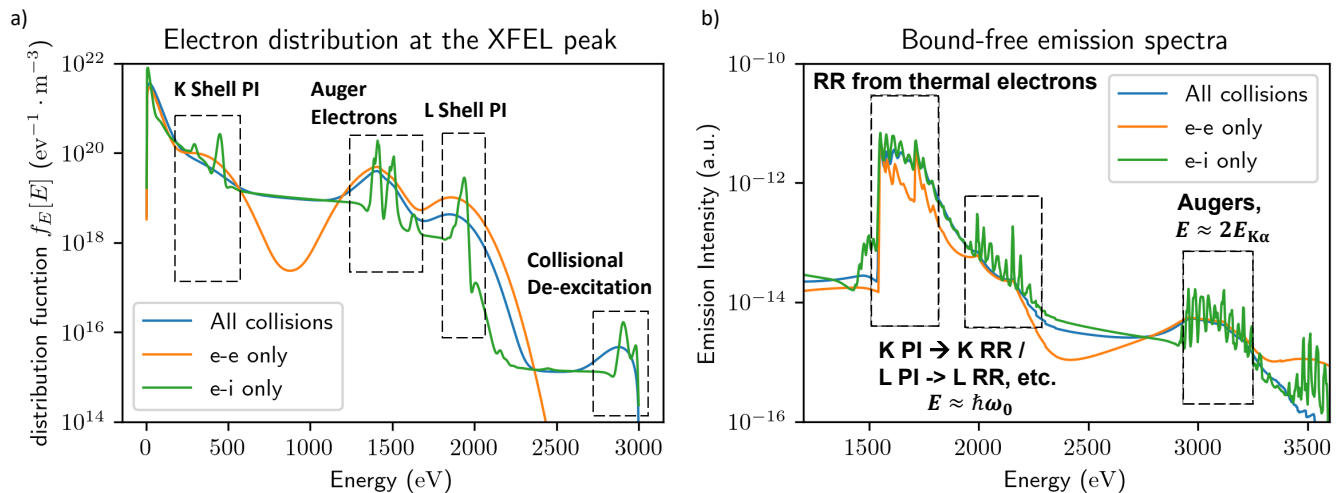


FIG. 7. Contribution of e-i and e-e collisions to electron thermalization. The electron distribution function is shown in (a), and the corresponding emission spectrum in (b). Note how the e-e collisions primarily determine the shape of the emission spectrum, which is the main experimental observable.

rations are used to drive a system to the plasma state, and the emission spectrum is recorded. The electron relaxation timescale can then be determined by scanning across collisional models in the simulations until agreement with the experiment is reached.

The previous simulations assumed relaxation time determined by Huba's version of the Coulomb Logarithm. As a first step, we could expand this by adding additional models as shown in Fig. 8, but we quickly see that at the solid densities we are interested in, many models suffer from unphysical divergences. In practice, simulations deploying CL models, such as CCFLY, tend to check for such divergences and replace the CL with a constant (often  $\ln[\Lambda] = 1$ ) once it starts approaching 0. So, rather than using different CL models to show the impact on relaxation timescales, we will scale the Huba relaxation time of  $\sim 0.2$  fs instead.

We performed two sets of simulations where the elastic e-e collision operator in Eq. (2) is manually rescaled by a factor of 0.1 or 10. We again run simulations over a range of pulse durations and show the results for the emission spectra in Fig. 9. For all simulations, we have maintained the normal cross-section for all e-i collisions; these are not affected by any scaling factor. We are primarily interested in how the spectra change as a function of e-e collisional rates only. When the relaxation time is made 10 times faster than that of the Huba model, even the shortest simulated XFEL pulse of 0.1 fs cannot detect any noticeable non-thermal features in the emission spectrum apart from the Auger knee just above 3 keV. We note that at present, x-ray pulse durations shorter than this are not readily accessible at XFEL facilities [49]. The contrasting case where the relaxation time is made longer (2 fs) than the XFEL pulse duration is shown in Fig. 9b. Here, the nonthermal emission features are clearly visible. For the shortest 0.1 fs x-ray pulses, we observe

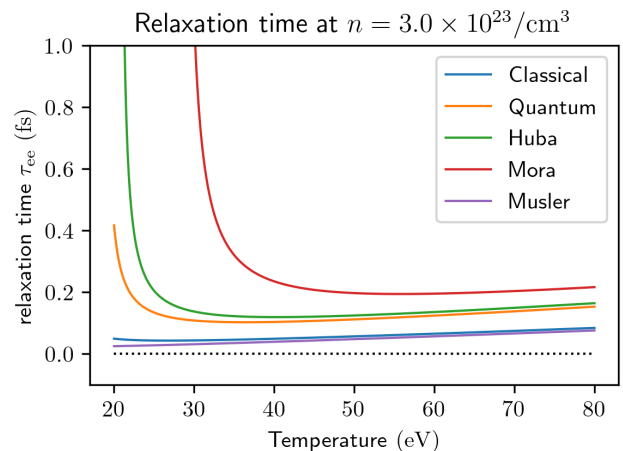


FIG. 8. Different Coulomb Logarithm models can lead to unphysically diverging relaxation times at high densities and low temperatures.

a multitude of satellite peaks, including from L-shell recombination. As non-thermal electrons persist for longer, many of them can recombine at a later time when various configurations of ions with a K shell core hole have appeared, resulting in richer emission features.

#### IV. CONCLUSIONS

In this study, we have described how the relaxation time of free electrons in the warm dense matter regime can be inferred from the emission spectra created by tailored non-thermal electron distributions. By varying the pulse duration of an ultra-short-pulse XFEL beam, the



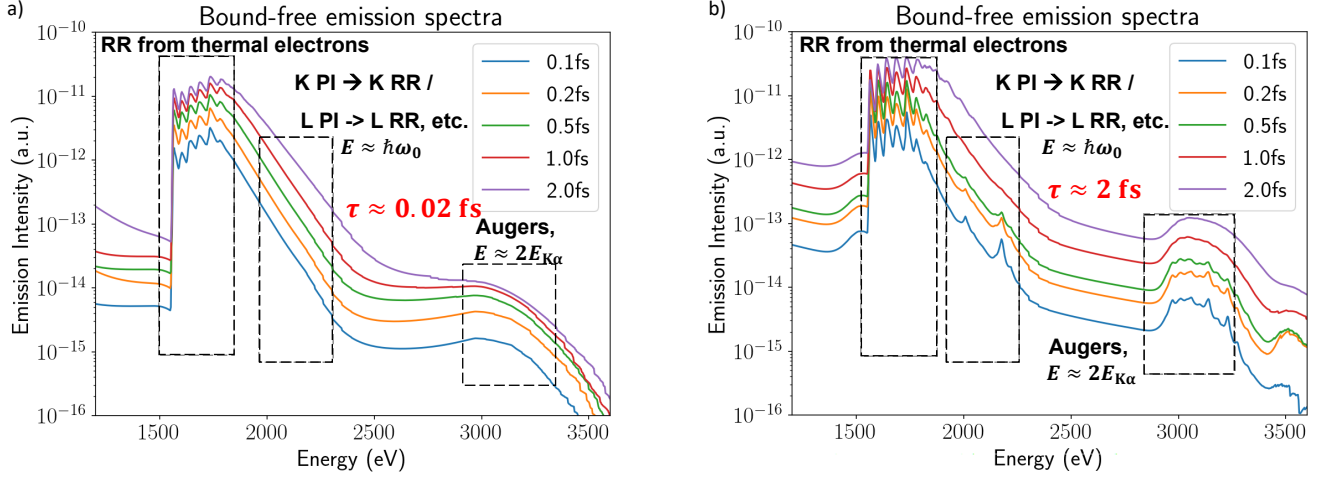


FIG. 9. Non-thermal features under different assumptions of e-e relaxation timescales. a). The relaxation is assumed to be 10 times as faster as that given by Huba's formula. The non-thermal features are weak even for the shortest pulse duration. b). The relaxation time is 0.1 times that of Huba, and non-thermal features are prominent. Note that even the L shell RR has appeared for this group of simulations.

thermalization process of non-thermal electrons can be observed and studied without the need for time-resolved measurements. For the non-thermal features to be prominent in the emission spectrum it is necessary for the x-ray pulse duration to be comparable in length to the typical e-e thermalization timescale. In warm-dense Al, this is expected to be on the order of 0.2 fs, but would be higher in mid- and high-Z materials driven at higher x-ray photon energies. The ability of modern XFELs to generate narrow-bandwidth, energetic attosecond pulses thus makes them ideally suited for such measurements. This work describes an approach that may soon be viable to

explore directly the validity of the e-e collisional models, including those based on the Coulomb Logarithm framework, in describing equilibration and transport in warm dense plasmas.

## ACKNOWLEDGMENTS

The authors acknowledge support from the UK EPSRC under grants EP/P015794/1 and EP/W010097/1. S.M.V. acknowledges support from the Royal Society.

- 
- [1] G. Chabrier, Plasma physics and planetary astrophysics, *Plasma Physics and Controlled Fusion* **51**, 124014 (2009).
  - [2] T. Guillot, Interiors of Giant Planets Inside and Outside the Solar System, *Science* **286**, 72 (1999).
  - [3] F. J. Rogers and C. A. Iglesias, *Astrophysical Opacity*, *Science* **263**, 50 (1994).
  - [4] J. D. Lindl, P. Amendt, R. L. Berger, S. G. Glendinning, S. H. Glenzer, S. W. Haan, R. L. Kauffman, O. L. Landen, and L. J. Suter, The physics basis for ignition using indirect-drive targets on the National Ignition Facility, *Physics of Plasmas* **11**, 339 (2004).
  - [5] D.-K. Kim and I. Kim, Calculation of ionization balance and electrical conductivity in nonideal aluminum plasma, *Physical Review E* **68**, 10.1103/physreve.68.056410 (2003).
  - [6] A. Ng, D. Parfeniuk, P. Celliers, L. DaSilva, R. M. More, and Y. T. Lee, Electrical Conductivity of a Dense Plasma, *Physical Review Letters* **57**, 1595 (1986).
  - [7] Y. T. Lee and R. More, An electron conductivity model for dense plasmas, *The Physics of fluids* **27**, 1273 (1984).
  - [8] C. E. Starrett, Coulomb log for conductivity of dense plasmas, *Physics of Plasmas* **25**, 10.1063/1.5053124 (2018).
  - [9] W. A. Stygar, G. Gerdin, and D. L. Fehl, Analytic electrical-conductivity tensor of a nondegenerate Lorentz plasma, *Physical review* **66**, 10.1103/physreve.66.046417 (2002).
  - [10] H. Reinholz, G. Röpke, S. Rosmej, and R. Redmer, Conductivity of warm dense matter including electron-electron collisions, *Physical Review E* **91**, 10.1103/physreve.91.043105 (2015).
  - [11] P. Balling and J. Schou, Femtosecond-laser ablation dynamics of dielectrics: basics and applications for thin films, *Reports on Progress in Physics* **76**, 036502 (2013).
  - [12] L. Jiang and H.-L. Tsai, Energy transport and material removal in wide bandgap materials by a femtosecond laser pulse, *International Journal of Heat and Mass Transfer* **48**, 487 (2005).
  - [13] K. Eidmann, J. Meyer-Ter-Vehn, T. Schlegel, and S. Hüller, Hydrodynamic simulation of subpicosecond laser interaction with solid-density matter, *Physical re-*

- view **62**, 1202 (2000).
- [14] L. Spitzer and R. Härm, Transport phenomena in a completely ionized gas, *Physical Review* **89**, 977 (1953).
  - [15] P. Mulser, G. Alber, and M. Murakami, Revision of the Coulomb logarithm in the ideal plasma, *Physics of Plasmas* **21**, 042103 (2014).
  - [16] M. Tzoufras, A. Bell, P. Norreys, and F. Tsung, A Vlasov–Fokker–Planck code for high energy density physics, *Journal of Computational Physics* **230**, 6475 (2011).
  - [17] P. Mora, Coulomb logarithm accuracy in a yukawa potential, *Phys. Rev. E* **102**, 033206 (2020).
  - [18] F. J. Blatt, *Solid state physics* (1957) pp. 199–366.
  - [19] T. E. Faber and J. Ziman, A theory of the electrical properties of liquid metals, *The philosophical magazine* **11**, 153 (1965).
  - [20] G. Röpke, Quantum-statistical approach to the electrical conductivity of dense, high-temperature plasmas, *Physical review* **38**, 3001 (1988).
  - [21] G. Röpke and R. Redmer, Electrical conductivity of non-degenerate, fully ionized plasmas, *Physical review* **39**, 907 (1989).
  - [22] R. Redmer, Physical properties of dense, low-temperature plasmas, *Physics Reports* **282**, 35 (1997).
  - [23] S. Kodanova, M. Issanova, S. Amirov, T. Ramazanov, A. Tikhonov, and Z. Moldabekov, Relaxation of non-isothermal hot dense plasma parameters, *Matter and Radiation at Extremes* **3**, 40 (2018).
  - [24] S. Ichimaru and S. Tanaka, Theory of interparticle correlations in dense, high-temperature plasmas. V. Electric and thermal conductivities, *Physical Review A* **32**, 1790 (1985).
  - [25] S. X. Hu, L. A. Collins, T. R. Boehly, J. D. Kress, V. N. Goncharov, and S. Skupsky, First-principles thermal conductivity of warm-dense deuterium plasmas for inertial confinement fusion applications, *Physical Review E* **89**, 10.1103/physreve.89.043105 (2014).
  - [26] D. O. Gericke, M. S. Murillo, and M. Schlenges, Dense plasma temperature equilibration in the binary collision approximation, *Physical Review E* **65**, 10.1103/physreve.65.036418 (2002).
  - [27] Q. Sun, J. Hong-Bing, Y. Liu, Z. Wu, H. Yang, and Q. Gong, Measurement of the collision time of dense electronic plasma induced by a femtosecond laser in fused silica, *Optics Letters* **30**, 320 (2005).
  - [28] C. Pan, L. Jiang, Q. Wang, J. Sun, G. Wang, and Y. Lu, Temporal-spatial measurement of electron relaxation time in femtosecond laser induced plasma using two-color pump-probe imaging technique, *Applied Physics Letters* **112**, 191101 (2018).
  - [29] T. R. Preston, S. M. Vinko, O. Ciricosta, P. Hollebon, H.-K. Chung, G. L. Dakovski, J. Krzywinski, M. Minitti, T. Burian, J. Chalupský, V. Hájková, L. Juha, V. Vozda, U. Zastrau, R. W. Lee, and J. S. Wark, Measurements of the  $k$ -shell opacity of a solid-density magnesium plasma heated by an x-ray free-electron laser, *Phys. Rev. Lett.* **119**, 085001 (2017).
  - [30] S. M. Vinko, V. Vozda, J. Andreasson, S. Bajt, J. Bielecki, T. Burian, J. Chalupsky, O. Ciricosta, M. P. Desjarlais, H. Fleckenstein, J. Hajdu, V. Hajkova, P. Hollebon, L. Juha, M. F. Kasim, E. E. McBride, K. Muehlig, T. R. Preston, D. S. Rackstraw, S. Roling, S. Toleikis, J. S. Wark, and H. Zacharias, Time-resolved xuv opacity measurements of warm dense aluminum, *Phys. Rev. Lett.* **124**, 225002 (2020).
  - [31] S. Vinko, G. Gregori, M. Desjarlais, B. Nagler, T. Whitcher, R. Lee, P. Audebert, and J. Wark, Free-free opacity in warm dense aluminum, *High Energy Density Physics* **5**, 124 (2009).
  - [32] P. Hollebon, O. Ciricosta, M. P. Desjarlais, C. Cacho, C. Spindloe, E. Springate, I. C. E. Turcu, J. S. Wark, and S. M. Vinko, Ab initio simulations and measurements of the free-free opacity in aluminum, *Phys. Rev. E* **100**, 043207 (2019).
  - [33] S. Toleikis, T. Bornath, T. Döppner, S. Düsterer, R. R. Fäustlin, E. Förster, C. Fortmann, S. H. Glenzer, S. Göde, G. Gregori, R. Irsig, T. Laarmann, H. J. Lee, B. Li, K.-H. Meiwes-Broer, J. Mithen, B. Nagler, A. Przystawik, P. Radcliffe, H. Redlin, R. Redmer, H. Reinholz, G. Röpke, F. Tavella, R. Thiele, J. Tiggesbäumker, I. Uschmann, S. M. Vinko, T. Whitcher, U. Zastrau, B. Ziaja, and T. Tschentscher, Probing near-solid density plasmas using soft x-ray scattering, *Journal of Physics B: Atomic, Molecular and Optical Physics* **43**, 194017 (2010).
  - [34] S. M. Vinko, O. Ciricosta, B. I. Cho, K. Engelhorn, H.-K. Chung, C. R. D. Brown, T. Burian, J. Chalupský, R. W. Falcone, C. Graves, V. Hájková, A. Higginbotham, L. Juha, J. Krzywinski, H. J. Lee, M. Messerschmidt, C. D. Murphy, Y. Ping, A. Scherz, W. Schlotter, S. Toleikis, J. J. Turner, L. Vysin, T. Wang, B. Wu, U. Zastrau, D. Zhu, R. W. Lee, P. A. Heimann, B. Nagler, and J. S. Wark, Creation and diagnosis of a solid-density plasma with an X-ray free-electron laser, *Nature* **482**, 59 (2012).
  - [35] A. Lévy, P. Audebert, R. Shepherd, J. Dunn, M. Cammarata, O. Ciricosta, F. Deneuville, F. Dorchies, M. Fajardo, C. Fourment, D. Fritz, J. Fuchs, J. Gaudin, M. Gauthier, A. Graf, H. J. Lee, H. Lemke, B. Nagler, J. Park, O. Peyrusse, A. B. Steel, S. M. Vinko, J. S. Wark, G. O. Williams, D. Zhu, and R. W. Lee, The creation of large-volume, gradient-free warm dense matter with an x-ray free-electron laser, *Physics of Plasmas* **22**, 030703 (2015).
  - [36] O. Ciricosta, S. M. Vinko, H.-K. Chung, C. Jackson, R. W. Lee, T. R. Preston, D. S. Rackstraw, and J. S. Wark, Detailed model for hot-dense aluminum plasmas generated by an x-ray free electron laser, *Physics of Plasmas* **23**, 022707 (2016).
  - [37] S. M. Vinko, O. Ciricosta, T. R. Preston, D. S. Rackstraw, C. Brown, T. Burian, J. Chalupský, B. I. Cho, H.-K. Chung, K. Engelhorn, R. W. Falcone, R. Fiokovini, V. Hájková, P. A. Heimann, L. Juha, H. J. Lee, R. W. Lee, M. Messerschmidt, B. Nagler, W. Schlotter, J. J. Turner, L. Vysin, U. Zastrau, and J. S. Wark, Investigation of femtosecond collisional ionization rates in a solid-density aluminium plasma, *Nature Communications* **6**, 10.1038/ncomms7397 (2015).
  - [38] S. Ren, Y. Shi, Q. Y. van den Berg, M. F. Kasim, H.-K. Chung, E. V. Fernandez-Tello, P. Velarde, J. S. Wark, and S. M. Vinko, Non-thermal evolution of dense plasmas driven by intense x-ray fields, *Communications Physics* **6**, 99 (2023).
  - [39] H.-K. Chung, M. Chen, W. Morgan, Y. Ralchenko, and R. Lee, FLYCHK: Generalized population kinetics and spectral model for rapid spectroscopic analysis for all elements, *High Energy Density Physics* **1**, 3 (2005).

- [40] H.-K. Chung, B. I. Cho, O. Ciricosta, S. M. Vinko, J. S. Wark, and R. W. Lee, Atomic processes modeling of X-ray free electron laser produced plasmas using SCFLY code, AIP Conference Proceedings 10.1063/1.4975712 (2017).
- [41] H.-K. Chung, M. Chen, and R. Lee, Extension of atomic configuration sets of the non-LTE model in the application to the  $K_\alpha$  diagnostics of hot dense matter, High Energy Density Physics **3**, 57 (2007).
- [42] Q. van den Berg, *Femtosecond electron dynamics in hot solid-density plasmas*, Ph.D. thesis, University of Oxford (2021).
- [43] M. N. Rosenbluth, W. M. MacDonald, and D. L. Judd, Fokker-Planck Equation for an Inverse-Square Force, Physical Review **107**, 1 (1957).
- [44] A. Bobylev and V. Chuyanov, On the numerical solution of Landau's kinetic equation, USSR Computational Mathematics and Mathematical Physics **16**, 121 (1976).
- [45] J. Sadler, Y. Lu, B. Spiers, M. W. Mayr, A. F. Savin, R. Wang, R. Aboushelbaya, K. Glize, R. Bingham, H. Li, K. Flippo, and P. Norreys, Kinetic simulations of fusion ignition with hot-spot ablator mix, Physical review **100**, 10.1103/physreve.100.033206 (2019).
- [46] W. Lotz, An empirical formula for the electron-impact ionization cross-section, The European Physical Journal A **206**, 205 (1967).
- [47] H. Van Regemorter, Rate of collisional excitation in stellar atmospheres., The Astrophysical Journal **136**, 906 (1962).
- [48] N. R. Huba, *NRL Plasma Formulary* (Naval Research Laboratory, Washington, 2013).
- [49] LCLS FEL Parameters (2022).